



[6]. A key issue surrounding the use of nanoelectronic devices [7], nano-enabled energy systems [8], and nanomedicine [9] is that of thermal management [10, 11]. The ability to successfully manipulate heat can be vital to device performance [12] and a lack of thermal regulation can lead to melting and device failure [13]. Understanding nanoscale heat transfer and phase change is therefore crucial for current and future applications of nanotechnology.

At the nanoscale, heat transfer and phase change become markedly different from their macroscopic counterparts. This is partially attributed to the increased ratio of surface-to-bulk atoms, which can introduce a size dependence to key thermodynamic parameters such as melt temperature [14–16], latent heat [17–19], and surface energy [20]. Furthermore, the mean free path of thermal energy carriers, known as phonons, can be on the order of hundreds of nanometers in crystalline solids at room temperature [11]. As a result, thermal transport on the nanoscale occurs as a ballistic process that is driven by infrequent collisions between phonons, in contrast to macroscopic thermal transport, which is a diffusive process driven by frequent collisions and gradients in the temperature. The ballistic nature of nanoscale heat transport can lead to substantial decreases in the effective thermal conductivity of nanomaterials, which has been experimentally confirmed [11, 21, 22] in samples with length scales up to 10 microns [23], far beyond the nano-regime.

Extensive research has been carried out to develop practical theories of heat transport and phase change that are valid at the nanoscale. The role of size-dependent parameters in nanoparticle [24–29] and nanowire [30, 31] melting has been studied using Fourier-based models of heat conduction [32]. However, models that are derived from Fourier’s law can only capture diffusive thermal transport and lead to an infinite speed of heat propagation, in clear contrast to the ballistic nature of nanoscale heat transport observed in experiments. Several approaches have been aimed at addressing this shortcoming [33]. Cattaneo [34] proposed that a temperature gradient can only induce a thermal flux after a finite amount of time has passed. An expansion of the governing equations about small relaxation times leads to the hyperbolic heat equation (HHE), or Maxwell–Cattaneo equation, which captures the wave-like propagation of heat associated with ballistic transport. Although the HHE correctly describes heat propagation with finite speed, the introduction of a relaxation time is somewhat ad-hoc and masks the underlying physics of nanoscale thermal transport. Guyer and Krumhansl [35, 36] later derived from the linearised Boltzmann transport equation an extension to the HHE which includes non-local effects and explicitly incorporates the phonon mean free path into the governing equations. The Guyer–Krumhansl (GK) equation is particularly appealing from a theoretical point of view because it provides a link between kinetic and continuum models and is based on well-defined physical parameters. Moreover, the striking similarity between the GK and Navier–Stokes equations enables nanoscale heat transport to be conceptualised in terms of fluid mechanics and this analogy has been used to rationalise the reduced thermal conductivity of nanosystems in terms of phonon hydrodynamics [33, 37, 38].

Theoretical studies of nanoscale phase change that incorporate non-Fourier heat transport are predominantly based on the HHE and originally focused on mathematical issues [39–41] and the correct form of boundary conditions [42, 43]. Solomon *et al.* [44] developed an enthalpy formulation of the hyperbolic Stefan problem and used numerical simulations to show that increasing the relaxation time can alter the solidification kinetics. Liu *et al.* [45] compared the parabolic (classical) and hyperbolic Stefan problems in the context of thermal spray particles and concluded that flux relaxation only influences the early stages of solidification, which agrees with the earlier work by Sadd and Didlake [46]. As shown by Mullis [47], hyperbolic heat transport can strongly influence the formation of dendrites in rapidly solidifying metal baths. Recently, the hyperbolic Stefan model has been applied to solidification problems arising in pulsed-laser surface treatment [48], cryopreservation of skin [49] and other biological tissues [50], and cryosurgery of lung cancer [51]. Sobolev [52] derived the GK equation from a two-temperature model and coupled it to the Stefan condition to study ultra-fast melting and solidification in the context of pulsed-laser experiments. This study, however, was restricted to the case of constant interface velocities and travelling-wave solutions for the temperature and flux.

In this paper, we carry out a detailed investigation of nanoscale solidification by coupling the GK equation to the Stefan condition. Matched asymptotic expansions are used to solve the free boundary problem without prior assumptions about the form of the solution and interface velocity. The systematic asymptotic analysis clearly elucidates the relationship between non-Fourier heat transport and the kinetics of solidification, and demonstrates the occurrence of large deviations from the classical behaviour predicted by Fourier’s law. To the best of our knowledge, this is the first time that matched asymptotic expansions have been used to study non-Fourier Stefan problems.

The paper is organised as follows. In Sec. 2, a one-phase model for one-dimensional nanoscale solidification is presented. The model focuses on heat conduction through the solid as described by the GK equation. Asymptotic solutions to the one-phase model are computed in Sec. 3 and used to understand how non-Fourier heat transport affects the solidification process. The paper concludes in Sec. 4.

## 2 Model formulation

We consider the growth of a nanoscale solid into a semi-infinite liquid bath, as depicted in Fig. 1. We will assume that one side of the bath is exposed to a cold environment that is held at a temperature  $T_e$  that is below the freezing temperature  $T_f$ . The solidification process will, therefore, be solely driven by the transfer of heat from the bath into the environment. Newton’s law will be used to model the exchange of thermal energy between the solid and surrounding environment. The model will consist of a conservation equations for thermal energy, the GK

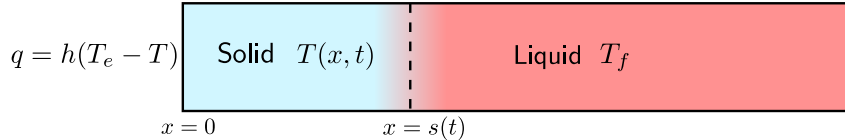


**Figure 1:** The solidification of a semi-infinite liquid bath that is in contact with a cold environment with temperature  $T_e$ . The transfer of heat from bath into the environment drives the solidification process and is modelled using a Newton boundary condition with a heat transfer coefficient  $h$ . The position of the planar solid-liquid interface is denoted by  $x = s(t)$ .

equation for the thermal flux, and appropriate boundary and initial conditions.

We will restrict our attention to one-dimensional dynamics and thus only consider planar solid-liquid interfaces. Furthermore, the initial temperature of the liquid bath is taken to be equal its freezing temperature  $T_f$ . As discussed below, this will allow us to study a one-phase model. Although this is a highly idealised situation, the simplicity of this configuration will facilitate the mathematical analysis and provide greater insights into the roles of nanoscale physics in solidification processes. The governing equations are written in terms of a Cartesian coordinate  $x$  describing the distance between the exposed solid surface and material points in the solid and bath, and a time variable  $t$ . The position of the solid-liquid interface, or solidification front, will be denoted by  $s(t)$ .

In this one-dimensional Cartesian setting, the temperature of the liquid will remain spatially uniform and equal to  $T_f$ , and the thermal flux through the liquid will be zero. Thus, the liquid will not play a role in the solidification process. Consequently, it is sufficient to consider a one-phase model involving only the solid. If the initial temperature of the bath is greater than the freezing temperature, then a two-phase model is required to capture the transfer of thermal energy from the liquid into the solid, which is expected to reduce the rate of solidification.

## 2.1 Bulk equations

Conservation of thermal energy provides an evolution equation for the solid temperature  $T$  given by

$$\rho c_p \frac{\partial T}{\partial t} + \frac{\partial q}{\partial x} = 0, \quad (1)$$

where  $\rho$  and  $c_p$  are the density and specific heat at constant pressure, respectively. The thermal flux of the solid,  $q$ , evolves according to the one-dimensional GK equation,

$$\tau_r \frac{\partial q}{\partial t} + q + k \frac{\partial T}{\partial x} = 3l^2 \frac{\partial^2 q}{\partial x^2}, \quad (2)$$

where  $\tau_r$  is the relaxation time,  $k$  is the bulk thermal conductivity, and  $l$  is the phonon mean free path (MFP). The first term on the left-hand side of the GK equation (2) captures memory effects and the delayed response of the flux to a change in thermal environment. The right-hand

side of the GK equation captures non-local effects due to phonon collisions. Taking  $\tau_r \rightarrow 0$  and  $l \rightarrow 0$  or, equivalently,  $t \gg \tau_r$  and  $x \gg l$ , in (2) recovers Fourier’s law,  $q = -k\partial T/\partial x$ . The various limits of the GK equation and its relationship to more general transport models are discussed in Sobolev [53].

In principle, all of the physical parameters in the bulk equations (1)–(2) can depend on the temperature and possibly the temperature gradient [33]; however, they are assumed to be constant. The GK equation (2) bears a marked resemblance to the one-dimensional Navier-Stokes equation (with a linear drag term). The temperature and flux play the respective roles of the pressure and fluid velocity, and the phonon MFP acts as a ‘thermal viscosity’, providing resistance to flux gradients.

## 2.2 Boundary conditions

To isolate the impact of non-Fourier heat conduction on the solidification kinetics, we use classical forms of the boundary conditions. The Newton condition at  $x = 0$ , describing the exchange of thermal energy between the cold environment and the solid, is given by

$$q = h(T_e - T), \quad x = 0, \quad (3)$$

where  $h$  is a heat transfer coefficient. The temperature at the interface is taken to be equal to the freezing temperature,

$$T = T_f, \quad x = s(t). \quad (4)$$

Finally, a balance of thermal energy across the solid-liquid interface yields the Stefan condition given by

$$\rho L_m \frac{ds}{dt} = -q, \quad x = s(t), \quad (5)$$

where  $L_m$  is the latent heat of solidification.

Non-classical boundary conditions would account for the finite time that is required for the temperature and flux to respond to a change in thermal environment [54]. In terms of the Newton condition (3), accounting for this delay amounts to adding  $\tau_r dq/dt$  to the left-hand side. Similarly, relaxation effects can lead to overheating [52, 55], whereby the temperature at the interface exceeds the equilibrium solidification temperature  $T_f$ , and can lead to modifications of the Stefan condition as well [54]. We leave the study of non-classical boundary conditions as an area of future work.

## 2.3 Initial conditions

It is assumed that solidification begins from a small seed crystal of width  $s_c$  that has formed, for example, by heterogeneous nucleation, at the wall of the bath. We take the initial temperature

of the seed crystal to be equal to the freezing temperature and the thermal flux throughout the crystal to be zero. Thus,

$$T(x, 0) = T_f, \quad q(x, 0) = 0, \quad s(0) = s_c. \quad (6)$$

A key distinction between classical and non-classical solidification problems is the role of the seed crystal. Classical problems capture the macroscopic dynamics on length scales that are typically much larger than those of the seed crystal and its size can be taken to be zero. The aim of non-classical models is to describe heat transfer on small length scales that are comparable to solid nuclei and, consequently, non-classical problems become dependent on the size of the seed crystal.

## 2.4 Non-dimensionalisation

The problem is non-dimensionalised by defining a temperature scale  $\Delta T = T_f - T_e > 0$ . The thermal flux is driven by the temperature difference between the fluid and the adjacent cold environment. This motivates choosing a scale for the flux by balancing terms in the Newton boundary condition (3), leading to  $q \sim h\Delta T$ . This choice allows the decrease in temperature near the environment to be captured, regardless of the size of the heat transfer coefficient  $h$ . There are multiple choices for the length scale, including the size of the seed crystal  $s_c$ . However, given that Fourier's law will eventually be recovered on length scales exceeding that of the seed crystal, we balance  $q$  and  $k \partial T / \partial x$  in the GK equation (2), yielding a length scale of  $x \sim k/h$ . This choice will facilitate comparing the classical and non-classical models. Finally, a time scale is chosen by balancing terms in the energy equation (1), giving  $t \sim \rho c_p k / h^2$ . Upon writing  $x = (k/h)x'$ ,  $t = (\rho c_p k / h^2)t'$ ,  $T = T_f + (\Delta T)T'$ , and  $q = (h\Delta T)q'$  in the governing equations (1)–(6), the non-dimensional equations (upon dropping the prime) are given by

$$\frac{\partial T}{\partial t} + \frac{\partial q}{\partial x} = 0, \quad (7a)$$

$$\gamma \frac{\partial q}{\partial t} + q + \frac{\partial T}{\partial x} = \ell^2 \frac{\partial^2 q}{\partial x^2}, \quad (7b)$$

with boundary conditions

$$q = -(1 + T), \quad x = 0, \quad (7c)$$

$$T = 0, \quad x = s(t). \quad (7d)$$

The Stefan condition is

$$\beta \frac{ds}{dt} = -q, \quad x = s(t), \quad (7e)$$

and the dimensionless initial conditions are

$$T = 0, \quad q = 0, \quad s = \varepsilon; \quad t = 0. \quad (7f)$$

The four dimensionless parameters that appear in the governing equations are defined by

$$\beta = \frac{L_m}{c_p \Delta T}, \quad \gamma = \frac{\tau_r h^2}{\rho c_p k}, \quad \ell = \frac{3^{1/2} l h}{k}, \quad \varepsilon = \frac{s_c h}{k}, \quad (8)$$

corresponding to the Stefan number, normalised relaxation time, MFP, and seed crystal size, respectively.

## 2.5 Model reformulations

In some cases, the asymptotic analysis proceeds more straightforwardly if the GK equation (7b) is re-written as

$$\gamma \frac{\partial q}{\partial t} + q + \frac{\partial T}{\partial x} = -\ell^2 \frac{\partial}{\partial t} \left( \frac{\partial T}{\partial x} \right), \quad (9)$$

which is obtained by first differentiating the energy equation (7a) with respect to  $x$  and using the result to eliminate the  $\partial^2 q / \partial x^2$  term in (7b). In the limit of zero relaxation time,  $\gamma \rightarrow 0$ , the GK equation (9) becomes

$$q = -\frac{\partial T}{\partial x} - \ell^2 \frac{\partial}{\partial t} \left( \frac{\partial T}{\partial x} \right), \quad (10)$$

indicating that non-local effects can drive, or inhibit, the thermal flux through temporal changes in the temperature gradient. By decomposing the flux  $q$  into its Fourier component  $-\partial T / \partial x$  and a non-classical component  $j$ , so that  $q = -\partial T / \partial x + j$ , the bulk equations can be written as

$$\frac{\partial T}{\partial t} - \frac{\partial^2 T}{\partial x^2} = -\frac{\partial j}{\partial x}, \quad (11a)$$

$$\frac{\partial j}{\partial t} + \gamma^{-1} j = (1 - \ell^2 / \gamma) \frac{\partial}{\partial t} \left( \frac{\partial T}{\partial x} \right). \quad (11b)$$

The initial conditions (7f) imply that  $j(x, 0) = 0$ . From (11), it is straightforward to see that  $j$  satisfies an ordinary differential equation in time; therefore, only two boundary conditions for this problem are required, either for the temperature, flux, or a combination of these two quantities. If the dimensionless relaxation time and MFP are such that  $\ell^2 / \gamma = 1$ , then solutions of the classical heat equation, based on Fourier's law, are solutions to the non-classical model (11), implying that non-classical effects do not lead to any distinguishing behaviour in this case. Consequently, setting  $\ell^2 / \gamma = 1$  in the asymptotic solutions will enable the Fourier solutions to be easily recovered. It has been shown that if  $\ell^2 / \gamma > 1$ , then the temperature is dominated by diffusion; if  $\ell^2 / \gamma < 1$ , then the temperature propagates as a wave [56–58].

## 2.6 Numerical method

To validate the asymptotic analysis, the full non-dimensional model (7) is numerically solved using a semi-implicit finite difference method. The temperature  $T$  and flux  $q$  are treated implicitly while the position  $s$  and speed  $ds/dt$  of the solidification front are treated explicitly;

see, for example, Font *et al.* [26] for further details. This approach effectively decouples the solidification and transport processes, allowing  $T$  and  $q$  to be (implicitly) updated for known  $s$  and  $ds/dt$ , and then  $s$  and  $ds/dt$  to be (explicitly) updated with the new flux  $q$ . The change of variable  $\eta = x/s(t)$  is used to transform the growing domain  $0 \leq x \leq s(t)$  to a fixed domain  $0 \leq \eta \leq 1$ . Second-order finite difference formulae are then used to discretise all spatial derivatives; central differences are used for interior grid points with forwards and backwards differences being employed when necessary for boundary grid points.

## 2.7 Parameter estimation

Tin is commonly used in theoretical and experimental studies of nanoscale heat transfer and phase change [16, 17, 29]. As a solid, tin has a density of  $\rho = 7180 \text{ kg/m}^3$ , a bulk thermal conductivity of  $k = 67 \text{ W/(m}\cdot\text{K)}$ , and specific heat of  $c_p = 230 \text{ J/(kg}\cdot\text{K)}$ . Tin solidifies at  $T_f = 505 \text{ K}$  and has a latent heat of  $L_m = 58500 \text{ J/kg}$ . The Stefan number can be parameterised in terms of the temperature difference  $\Delta T = T_f - T_e$  as  $\beta \simeq 254 \text{ K}/\Delta T$  and may be treated as large for moderate values of  $\Delta T$  up to 50 K. Similar conclusions are reached for other solidifying metals such as aluminium and nickel [45, 47]. To facilitate the analysis, we restrict our attention to the case of large Stefan numbers. The heat transfer coefficient  $h$  depends on the nature of the surrounding environment and can be difficult to estimate. Therefore, we follow Ribera and Myers [29] and take  $h = 4.7 \times 10^9 \text{ W/(m}^2\cdot\text{K)}$ , which provides the closest approximation to the fixed-temperature boundary condition that is thermodynamically reasonable [33]. Estimates of the phonon MFP range from 1 nm to 100 nm [10], with 40 nm being the ‘textbook’ value [23]. There is a similarly broad range of estimates for the relaxation time, which are typically on the order of  $10^{-12} \text{ s}$  to  $10^{-10} \text{ s}$  [45, 59]. This leads to dimensionless relaxation times ranging from  $\gamma = 0.2$  to  $\gamma = 20$  and dimensionless MFPs of  $\ell = 0.12$  to  $\ell = 120$ . The dimensionless seed crystal size is more difficult to estimate; however, given that  $k^s/h$  defines a length scale of 14 nm, we assume that  $\varepsilon$  is small.

## 3 Asymptotic analysis

The presumed largeness of the Stefan number and the wide range of values for the dimensionless relaxation time and MFP can be exploited to construct asymptotic approximations to the full model (7). The limit of large Stefan number corresponds to the time scale of thermal diffusion being much smaller than the time scale of interface motion. This is typical for many materials and physical scenarios. Consequently, it is possibly the most common approach for simplifying theoretical models of phase change. The relatively fast thermal diffusion rate implies that, on the time scale of interface motion, the temperature can be well approximated by its quasi-steady profile. In many cases, an analytical solution for the quasi-steady temperature profile can be obtained, reducing the Stefan problem to an ordinary differential equation for the position of



the free boundary; see, for example, Myers *et al.* [26, 29, 30]. In Sec. 3.1, we consider the case when non-dimensional relaxation time,  $\gamma$ , and MFP,  $\ell$ , are order one or smaller. The solidification kinetics are well described by the classical solution, indicating that non-Fourier heat conduction does not play a large role in this parameter regime. The cases when  $\ell \gg 1$  and  $\gamma \gg 1$  are considered in Sec. 3.2 and Sec. 3.3, respectively. Substantial deviations from the classical solidification kinetics are found in these cases.

### 3.1 Order-one relaxation time and MFP

We consider the asymptotic limit as  $\beta \rightarrow \infty$  with  $\varepsilon \ll \beta^{-1}$ . There are four key time regimes to consider. The first, given by  $t = O(\varepsilon^2)$ , describes the initial cooling of the seed crystal and it captures the transient development of the temperature gradient and thermal flux. The dynamics in this regime are dominated by non-classical effects. Remarkably, however, the governing equations reduce to Fourier's law with an effective thermal conductivity that depends on the dimensionless relaxation time and MFP. The second time regime,  $t = O(\varepsilon\beta)$ , captures the initial growth of the solid. The temperature has a quasi-steady profile with a constant gradient (in time and space) that differs from the classical case. In the third regime,  $t = O(1)$ , non-local effects drive the temperature and flux to their classical profiles. In essence, the third regime captures the transition from non-classical to classical heat conduction. The size of the solid remains relatively unchanged up to this point. Finally, the fourth time regime,  $t = O(\beta)$ , captures the quasi-steady growth of the solid. Non-classical effects are small on this large time scale and the classical quasi-steady Stefan problem is recovered at leading order.

*First time regime:* The variables are rescaled in order to capture the evolution of the temperature and flux from their initial conditions on a length scale that coincides with the initial size of the solid. Thus, we choose a length scale of  $O(\varepsilon)$  and rescale time, temperature, and flux to ensure that the time derivatives of the latter two quantities enter the leading-order problem. This leads to a rescaling given by  $t = \varepsilon^2 \tilde{t}$ ,  $x = \varepsilon \tilde{x}$ ,  $s = \varepsilon \tilde{s}$ ,  $T = \varepsilon \tilde{T}$ , and  $q = \tilde{q}$ . The leading-order bulk equations are

$$\frac{\partial \tilde{T}}{\partial \tilde{t}} + \frac{\partial \tilde{q}}{\partial \tilde{x}} = 0, \quad (12a)$$

$$\gamma \frac{\partial \tilde{q}}{\partial \tilde{t}} = -\ell^2 \frac{\partial}{\partial \tilde{t}} \left( \frac{\partial \tilde{T}}{\partial \tilde{x}} \right), \quad (12b)$$

subject to  $\tilde{T} = \tilde{q} = 0$  at  $\tilde{t} = 0$ . Upon integration of (12b) in time and imposing the initial conditions, we find that  $\tilde{q} = -(\ell^2/\gamma)\partial\tilde{T}/\partial\tilde{x}$ , recovering Fourier's law with an effective thermal conductivity  $\ell^2/\gamma$  that depends on non-classical parameters. The leading-order Stefan condition is given by  $d\tilde{s}/d\tilde{t} = 0$ , with  $\tilde{s}(0) = 1$ , indicating that crystal growth is negligible on this time scale. The leading-order problem is simply a classical heat conduction problem on a fixed

domain:

$$\frac{\partial \tilde{T}}{\partial \tilde{t}} = \frac{\ell^2}{\gamma} \frac{\partial^2 \tilde{T}}{\partial \tilde{x}^2}, \quad (13a)$$

subject to

$$\frac{\ell^2}{\gamma} \frac{\partial \tilde{T}}{\partial \tilde{x}} = 1, \quad \tilde{x} = 0, \quad (13b)$$

$$\tilde{T} = 0, \quad \tilde{x} = 1, \quad (13c)$$

$$\tilde{T} = 0, \quad \tilde{t} = 0. \quad (13d)$$

The large-time limit of the solution to (13), the flux, and the position of the solidification front, written in terms of the original dimensionless variables, is given by

$$T \sim -(\gamma/\ell^2)(\varepsilon - x), \quad q \sim -1, \quad s \sim \varepsilon, \quad (14)$$

which will be used to match into the next time regime.

*Second time regime:* The second time regime is defined by  $t = O(\varepsilon\beta)$ , which arises from balancing terms in the Stefan condition given that  $q = O(1)$  and  $s = O(\varepsilon)$  from the matching condition (14). Furthermore, the matching condition for the temperature implies that  $T = O(\varepsilon)$  (recall that  $\gamma/\ell^2 = O(1)$ ). The variables are therefore rescaled according to  $x = \varepsilon\bar{x}$ ,  $s = \varepsilon\bar{s}$ , and  $T = \varepsilon\bar{T}$ . We also write  $q = -1 + \varepsilon\bar{q}$  to ensure the matching condition is satisfied and to balance terms in the Newton boundary condition. The rescaled bulk equations become

$$\frac{\partial \bar{q}}{\partial \bar{x}} = O(\beta^{-1}), \quad (15a)$$

$$\frac{\partial}{\partial \bar{t}} \left( \frac{\partial \bar{T}}{\partial \bar{x}} \right) = O(\varepsilon\beta), \quad (15b)$$

and the boundary conditions are  $\bar{q} = -\bar{T}$  at  $\bar{x} = 0$  and  $\bar{T} = 0$  at  $\bar{x} = \bar{s}(\bar{t})$ . The relevant matching conditions are given by  $\bar{T} \sim -(\gamma/\ell^2)(1 - \bar{x})$  and  $\bar{s} \sim 1$  as  $\bar{t} \sim 0$ . Solving the leading-order problem yields the solution

$$\bar{T}(\bar{x}, \bar{t}) = -(\gamma/\ell^2)(\bar{s}(\bar{t}) - \bar{x}), \quad (16a)$$

$$\bar{q}(\bar{x}, \bar{t}) = (\gamma/\ell^2)\bar{s}(\bar{t}), \quad (16b)$$

$$\bar{s}(\bar{t}) = 1 + \bar{t}. \quad (16c)$$

For  $\bar{t} \gg 1$ , the leading-order solution (16) can be written in terms of the original non-dimensional variables as  $T \sim -\beta^{-1}(\gamma/\ell^2)(t - \beta x)$ ,  $q \sim -1 + \beta^{-1}(\gamma/\ell^2)t$ , and  $s \sim \beta^{-1}t$ .

*Third time regime:* The scales for the third regime,  $t = O(1)$ , arise from the  $\bar{t} \gg 1$  limit of the solution in the second time regime and, in essence, promote the  $O(\varepsilon\beta)$  terms in (15b) to leading order. The time scale of  $t = O(1)$  is determined by balancing terms in the GK equation (7b) given that  $s \sim \beta^{-1}t$ ,  $T \sim \beta^{-1}t$ , and  $q \sim -1 + \beta^{-1}t$ . The variables are then rescaled as  $t = \hat{t}$ ,

$x = \beta^{-1}\hat{x}$ ,  $s = \beta^{-1}\hat{s}$ ,  $T = \beta^{-1}\hat{T}$ , and  $q = -1 + \beta^{-1}\hat{q}$ . The energy equation is given by  $\partial\hat{q}/\partial\hat{x} = O(\beta^{-1})$ . Similarly, the rescaled GK equation reads  $-1 + \partial\hat{T}/\partial\hat{x} = -\ell^2\partial(\partial\hat{T}/\partial\hat{x})/\partial\hat{t} + O(\beta^{-1})$ , corresponding to an extension of Fourier's law (the left-hand side) that includes non-local effects (the right-hand side). The boundary conditions are  $\hat{q}(0, \hat{t}) = -\hat{T}(0, \hat{t})$  and  $\hat{T}(\hat{s}(\hat{t}), \hat{t}) = 0$ , and the Stefan condition is  $d\hat{s}/d\hat{t} = 1 + O(\beta^{-1})$ . The relevant matching conditions are  $\hat{T} \sim -(\gamma/\ell^2)(\hat{t} - \hat{x})$ ,  $\hat{q} \sim (\gamma/\ell^2)\hat{t}$ , and  $\hat{s} \sim \hat{t}$  as  $\hat{t} \sim 0$ . The leading-order solutions for the temperature, the flux, and the position of the solidification front are

$$\hat{T}(\hat{x}, \hat{t}) = -(\hat{s}(\hat{t}) - \hat{x}) \left[ 1 - (1 - \gamma/\ell^2)e^{-\hat{t}/\ell^2} \right] \quad (17a)$$

$$\hat{q}(\hat{x}, \hat{t}) = \hat{s}(\hat{t}) \left[ 1 - (1 - \gamma/\ell^2)e^{-\hat{t}/\ell^2} \right], \quad (17b)$$

$$\hat{s}(\hat{t}) = \hat{t} \quad (17c)$$

The classical solution can be obtained by taking the limit  $\gamma/\ell^2 \rightarrow 1$ , which shows that pure Fourier conduction leads to a temperature profile with a constant gradient and a flux  $q \sim -1 + t$  that decreases (in magnitude) linearly in time. The role of non-classical effects is to introduce a time dependence that drives the temperature and flux to their classical profiles.

*Fourth time regime:* The fourth time regime captures the growth of the solid over long time scales. Balancing terms in the Stefan condition with  $s = O(1)$  and  $q = O(1)$  requires  $t = O(\beta)$ . Thus, time is written as  $t = \beta\tau$  and the other variables are unchanged. The rescaled problem is given by

$$\beta^{-1}\frac{\partial T}{\partial\tau} + \frac{\partial q}{\partial x} = 0, \quad (18a)$$

$$\beta^{-1}\gamma\frac{\partial q}{\partial t} + q + \frac{\partial T}{\partial x} = \ell^2\frac{\partial^2 q}{\partial x^2}, \quad (18b)$$

with boundary conditions

$$q = -(1 + T), \quad x = 0, \quad (18c)$$

$$T = 0, \quad x = s(\tau). \quad (18d)$$

The Stefan condition is

$$\frac{ds}{d\tau} = -q, \quad x = s(\tau), \quad (18e)$$

with matching conditions in time that will be specified below. Capturing the non-classical effects on this time scale requires the calculation of higher-order terms in the asymptotic expansions of the variables. Therefore, the solution to (18) is sought as an asymptotic expansion of the form  $T = T_0 + \beta^{-1}T_1 + O(\beta^{-2})$ ,  $q = q_0 + \beta^{-1}q_1 + O(\beta^{-2})$ , and  $s = s_0 + \beta^{-1}s_1 + O(\beta^{-2})$ .

The leading-order contribution to the energy equation (18a) shows that the flux is constant in space and given by  $q_0(x, \tau) \equiv -(1 + T_0(0, \tau))$ , which implies that the non-local terms drop out of the GK equation (18b). Moreover, due to the assumption that  $\gamma = O(1)$ , flux relaxation is also

a higher-order effect. The leading-order GK equation reduces to Fourier's law,  $q_0 = -\partial T_0/\partial x$ . The temperature profile and flux can be written as

$$T_0(x, \tau) = \frac{x - s_0(\tau)}{1 + s_0(\tau)}, \quad (19a)$$

$$q_0(x, \tau) = -\frac{1}{s_0(\tau) + 1}. \quad (19b)$$

Integrating the Stefan condition and using the matching condition  $s_0(0) = 0$  yields

$$s_0(\tau) = -1 + \sqrt{1 + 2\tau}. \quad (19c)$$

The leading-order solutions for the position of the solidification front (16c), (17c), and (19c) can be combined into a composite solution [60, 61] given by

$$s(t) = \varepsilon + \sqrt{1 + 2\beta^{-1}t} - 1, \quad (20)$$

which is valid for all times.

The next-order problem contains contributions from non-classical terms and can be written as

$$\frac{\partial T_0}{\partial \tau} + \frac{\partial q_1}{\partial x} = 0, \quad (21a)$$

$$\gamma \frac{dq_0}{d\tau} + q_1 + \frac{\partial T_1}{\partial x} = \ell^2 \frac{\partial^2 q_1}{\partial x^2}, \quad (21b)$$

with boundary conditions

$$q_1 = -T_1, \quad x = 0, \quad (21c)$$

$$T_1 = -\frac{\partial T_0}{\partial x} s_1, \quad x = s_0(\tau). \quad (21d)$$

The Stefan condition is given by

$$\frac{ds_1}{d\tau} = -q_1, \quad x = s_0(\tau). \quad (21e)$$

Matching to the solution in the first time regime gives that  $s_1(0) = 0$ . Before attempting to solve the problem, it is illustrative to first rewrite the GK equation (21b) using the solution for  $q_0$  and the fact that  $\partial^2 q_1/\partial x^2 = dq_0/d\tau$ , which yields

$$q_1 + \frac{\partial T_1}{\partial x} = (\gamma - \ell^2) \frac{d}{d\tau} \left( \frac{1}{s_0(\tau) + 1} \right) = -\frac{\gamma - \ell^2}{(s_0(\tau) + 1)^3}. \quad (22)$$

Therefore, the flux is simply given by Fourier's law with a time-dependent source term, the magnitude of which is characterised by the grouped parameter  $\gamma - \ell^2$ . Using (22), the flux  $q_1$  can be eliminated from the governing equations and the problem can be formulated solely in terms of the temperature  $T_1$ , as in the classical Stefan problem. Carrying out this process yields the system of equations given by

$$\frac{\partial^2 T_1}{\partial x^2} = \frac{\partial T_0}{\partial \tau}, \quad (23a)$$

with boundary conditions

$$\frac{\partial T_1}{\partial x} = T_1 + (\gamma - \ell^2) \frac{d}{d\tau} \left( \frac{1}{s_0(\tau) + 1} \right), \quad x = 0, \quad (23b)$$

$$T_1 = -\frac{s_1(\tau)}{s_0(\tau) + 1}, \quad x = s_0(\tau), \quad (23c)$$

and the Stefan condition

$$\frac{ds_1}{d\tau} = \frac{\partial T_1}{\partial x} - (\gamma - \ell^2) \frac{d}{d\tau} \left( \frac{1}{s_0(\tau) + 1} \right), \quad x = s_0(\tau). \quad (23d)$$

An analytical solution for the temperature  $T_1$  can be found and used in the Stefan condition to find that the correction to the solidification front evolves according to

$$\frac{ds_1}{d\tau} + \frac{s_1(\tau)}{(s_0(\tau) + 1)^2} = -\frac{1}{3} \left[ 1 - \frac{1}{(s_0(\tau) + 1)^3} \right] \frac{ds_0}{d\tau} + \frac{(\gamma - \ell^2) s_0}{(s_0(\tau) + 1)^3} \frac{ds_0}{d\tau}. \quad (24)$$

Equation (24) can be integrated and the solution for  $s_1$  can be written in terms of  $s_0$  as

$$s_1(\tau) = -\frac{1}{6} \frac{s_0(\tau)^2(3 + s_0(\tau))}{(s_0(\tau) + 1)^2} + (\gamma - \ell^2) \left[ \frac{\log(s_0(\tau) + 1)}{s_0(\tau) + 1} - \frac{s_0(\tau)}{(s_0(\tau) + 1)^2} \right]. \quad (25)$$

For small and large times,  $\tau \ll 1$  and  $\tau \gg 1$ , respectively, we find that

$$s_1 \sim \frac{1}{2} (\gamma - \ell^2 - 1) \tau^2, \quad \tau \ll 1, \quad (26a)$$

$$s_1 \sim -\frac{1}{6} \left( (2\tau)^{1/2} + 1 - \frac{3}{(2\tau)^{1/2}} \right) + \frac{\gamma - \ell^2}{(2\tau)^{1/2}} \left( \frac{1}{2} \log(2\tau) - 1 \right), \quad \tau \gg 1. \quad (26b)$$

Thus, for small times, the role of classical and non-classical effects in the correction to the position of the solidification front are comparable. However, for large times, non-classical effects become sub-dominant. This can be explained on physical grounds: on large time scales, the solid can grow far beyond the phonon MFP, reducing the influence of non-local effects, and the flux, like the temperature, will have relaxed to its quasi-steady state. Furthermore, both equations in (26) show that non-classical effects can either facilitate or inhibit solidification depending on the sign of  $\gamma - \ell^2$ . On one hand, a larger value of  $\gamma$  corresponds to a slower relaxation (i.e., increase) of the flux from its initial value of  $q_0 = -1$ , thereby enhancing thermal transport from the interface to the environment and accelerating the solidification process. On the other hand, the combination of non-local effects and a decreasing temperature gradient (in time) inhibit the transport of heat throughout the solid (see (10)), resulting in a slower solidification process as  $\ell$  is increased.

Figure 2 shows the representative dynamics that occur in the limit of large Stefan number, using  $\gamma = 1$ ,  $\beta = 10$ , and  $\varepsilon = 10^{-3}$ . Figure 2 (a) illustrates the evolution of the mean temperature gradient, defined by

$$\left\langle \frac{\partial T}{\partial x} \right\rangle \equiv \frac{T(s(t), t) - T(0, t)}{s(t)}, \quad (27)$$

for different values of  $\ell$ . As indicated by the asymptotic analysis, the temperature quickly settles into a linear profile; therefore, the mean temperature gradient contains all of the information about how the temperature profile evolves in time. Since the value of  $\gamma$  is fixed at  $\gamma = 1$ , the values of  $\ell = 0.5, 1.0$ , and  $1.5$  correspond to the three distinguishing cases:  $\gamma/\ell^2 > 1$ ,  $\gamma/\ell^2 = 1$  (Fourier), and  $\gamma/\ell^2 < 1$ , respectively. Compared to the Fourier case, the temperature gradients in the non-classical cases exhibit much richer dynamics as they evolve through the multiple time regimes that were elucidated by the asymptotic analysis. In the classical case, many of these regimes appear blended together because the temperature gradient remains constant in time with a value given by  $\partial T/\partial x = \gamma/\ell^2 = 1$ . When  $\gamma/\ell^2 > 1$  ( $\gamma/\ell^2 < 1$ ), the temperature profile initially has a stronger (weaker) gradient due to the reduced (enhanced) effective thermal conductivity of the solid. Non-local effects drive the temperature gradients to their classical value and all three curves converge when  $t \simeq 10 = O(\beta)$ . In the case of  $\ell = 0.5$ , the numerical approximation of the mean temperature gradient is compared with the asymptotic solutions in all four time regimes. Using the values of  $\beta = 10$  and  $\varepsilon = 10^{-3}$ , these four regimes are given by  $t \simeq 10^{-6}, 10^{-2}, 1$ , and  $10$ . Diamonds correspond to the numerical solution of (13), valid in the first regime, which describes the rapid initial development of the temperature gradient on  $t = O(\varepsilon^2)$  time scales. Stars, diamonds, and circles denote the asymptotic solutions (16a), (17a), and (19a) in the second, third, and fourth regimes, respectively. In all cases, the agreement between asymptotics and numerics is excellent.

Figure 2 (b) shows the evolution of the solidification front in the case when  $\ell = 0.5$ . Superposed on this panel is the logarithm of the flux,  $\log_{10}(-q)$ , which is uniform in space and decreases from  $q \simeq 1$  when  $t \simeq 10^{-3}$  to  $q \simeq 10^{-1}$  when  $t \simeq 10^3$ . The squares correspond to the leading-order composite solution for the position of the solidification front (20), which does not contain contributions from the non-classical terms associated with the GK equation. The excellent agreement between the asymptotic and numerical solutions confirms that non-classical effects do not play a significant role in the dynamics of solidification in this parameter regime. This is due to flux relaxation and non-local effects being negligible over the large time scales on which appreciable growth occurs.

### 3.2 Limit of large MFP

We now consider the asymptotic limit as  $\ell \rightarrow \infty$  and  $\beta \rightarrow \infty$  with  $\varepsilon \ll \beta^{-1} \ll 1$ . The relative sizes of  $\beta$  and  $\ell$  will be discussed further below. There are up to five time regimes to consider. The first two, defined by  $t = O(\varepsilon^2 \ell^{-2})$  and  $t = O(\beta \varepsilon)$ , describe the initial evolution of the temperature and flux due to the outflow of heat into the environment, and the growth of the solid on length scales associated with the seed crystal. The third and fourth regimes,  $t = O(1)$  and  $t = O(\ell \beta^{1/2})$ , essentially capture the same physics, whereby the flux is driven by temporal changes in the temperature gradient, but slightly differ in their mathematical structure. If  $\beta \ll \ell^2$ , then there is a fifth time regime,  $t = O(\ell^2)$ , which captures the transition to classical

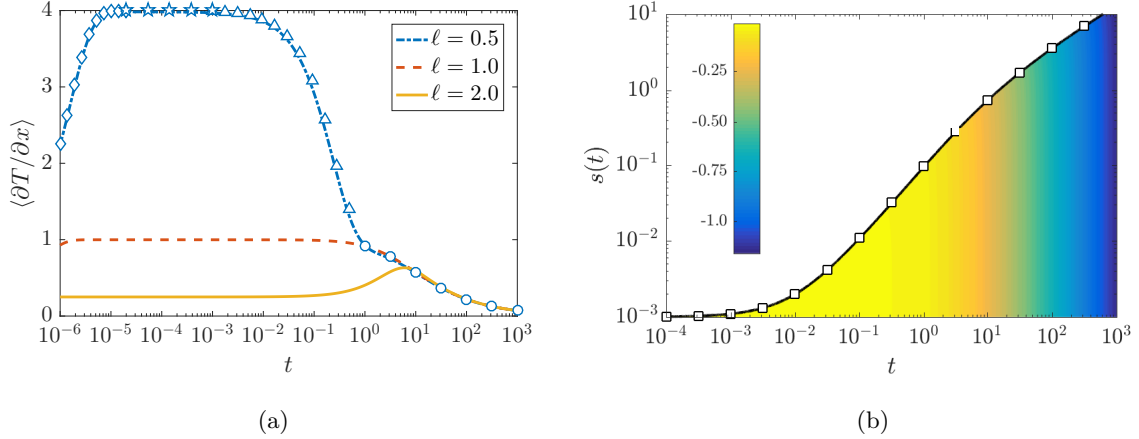


**Figure 2:** Solidification dynamics in the limit of large Stefan number. Left (a): Evolution of the mean temperature gradient  $\langle \partial T / \partial x \rangle \equiv [T(s(t), t) - T(0, t)]/s(t)$  for different values of  $\ell$  with a fixed value of  $\gamma = 1$ . Right (b): Evolution of the solidification front with the logarithm of the flux,  $\log_{10}(-q)$ , superposed as a colour gradient. Lines and diamonds represent numerical solutions of the full model (7) and the reduced model in the first time regime (13). Stars, triangles, circles, and squares correspond to (16a), (17a), (19a), and (20), respectively. In both panels,  $\gamma = 1$ ,  $\beta = 10$  and  $\varepsilon = 10^{-3}$ . A value of  $\ell = 0.5$  was used in panel (b).

quasi-static solidification, with a flux that is driven by temperature gradients.

*First and second time regimes:* The first two time regimes are mathematically identical to those previously considered when  $\ell = O(1)$ . The limiting behaviour is

$$T \sim -\gamma \ell^{-2} \beta^{-1} (s(t) - \beta x), \quad q \sim -1 + \gamma \ell^{-2} \beta^{-1} t, \quad s \sim \beta^{-1} t, \quad (28a)$$

for  $\beta \varepsilon \ll t \ll 1$ .

*Third time regime:* Scales for the temperature, flux, and the position of the solidification front (and hence space) can be obtained from the limiting behaviour in the second regime (28). The time scale is selected by balancing terms in the GK equation. The only sensible balance occurs between  $q = O(1)$  and  $\ell^{-2} \partial(\partial T / \partial x) / \partial t = O(t^{-1})$ , which requires  $t = O(1)$ , and implies that the flux is driven by temporal changes in the temperature gradient. Thus, the variables are rescaled as  $t = \hat{t}$ ,  $x = \beta^{-1} \hat{x}$ ,  $s = \beta^{-1} \hat{s}$ ,  $T = \ell^{-2} \beta^{-1} \hat{T}$ , and we write  $q = -1 + \ell^{-2} \beta^{-1} \hat{q}$ . The leading-order bulk equations are given by  $\partial(\partial \hat{T} / \partial \hat{x}) / \partial \hat{t} = 1$  and  $\partial \hat{q} / \partial \hat{x} = 0$ . Matching conditions for the temperature and solidification front are  $\hat{T} \sim -\gamma(\hat{s} - \hat{x})$  and  $\hat{s} \sim \hat{t}$  as  $\hat{t} \sim 0$ . Boundary conditions are  $\hat{q}(0, \hat{t}) = -(1 + \hat{T}(0, \hat{t}))$  and  $\hat{T}(\hat{s}(\hat{t}), \hat{t}) = 0$ . The Stefan condition is given by  $d\hat{s}/d\hat{t} = 1 + O(\ell^{-2} \beta^{-1})$ . The leading-order solution can be written as

$$\hat{T}(\hat{x}, \hat{t}) = -(\hat{t} + \gamma)(\hat{s}(\hat{t}) - \hat{x}), \quad (29a)$$

$$\hat{q}(\hat{x}, \hat{t}) = (\hat{t} + \gamma)\hat{s}(\hat{t}), \quad (29b)$$

$$\hat{s}(\hat{t}) = \hat{t}, \quad (29c)$$

which is consistent with the large- $\ell$  expansion of (17). Equation (29c) indicates that the growth kinetics of the solid are linear when  $t = O(1)$ , as in the case of classical Fourier conduction, despite the fact that the flux is driven by a non-classical mechanism. This is a result of the flux changing by only a very small amount in this time regime; recall that  $q = -1 + \ell^{-2}\beta^{-1}\bar{q}$ .

*Fourth time regime:* The fourth time regime is an extension of the third which captures  $O(1)$  changes in the flux; thus, we take  $q = O(1)$ . Balancing terms in the Newton condition under this assumption leads to  $T = O(1)$ . Length and time scales can be obtained by balancing both terms in the Stefan condition along with  $q$  and  $\partial(\partial T/\partial x)/\partial t$  in the GK equation, yielding  $x = O(\ell\beta^{-1/2})$  and  $t = O(\ell\beta^{1/2})$ . Therefore, the variables are rescaled as  $t = \ell\beta^{1/2}\bar{t}$ ,  $x = \ell\beta^{-1/2}\bar{x}$ ,  $s = \ell\beta^{-1/2}\bar{s}$ ,  $T = \bar{T}$ , and  $q = \bar{q}$ . The rescaled energy and GK equations can be written as

$$\frac{\partial \bar{q}}{\partial \bar{x}} = O(\beta^{-1}), \quad (30a)$$

$$\ell^{-1}\beta^{-1/2}\gamma\frac{\partial \bar{q}}{\partial \bar{t}} + \bar{q} + \alpha\frac{\partial \bar{T}}{\partial \bar{x}} = -\frac{\partial}{\partial \bar{t}}\left(\frac{\partial \bar{T}}{\partial \bar{x}}\right), \quad (30b)$$

where  $\alpha = \ell^{-1}\beta^{1/2}$ . For the moment, we will assume that  $\alpha = O(1)$ . The matching conditions for this problem are given by  $\bar{T} \sim -\bar{t}(\bar{s}(\bar{t}) - \bar{x})$  and  $\bar{s} \sim \bar{t}$  as  $\bar{t} \sim 0$ . Differentiation of the GK equation with respect to  $\bar{x}$  yields an evolution equation for the curvature of the temperature profile,

$$\frac{\partial}{\partial \bar{t}}\left(\frac{\partial^2 \bar{T}}{\partial \bar{x}^2}\right) = -\alpha\frac{\partial^2 \bar{T}}{\partial \bar{x}^2}. \quad (31)$$

From the matching condition,  $\partial^2 \bar{T}/\partial \bar{x}^2 \sim 0$  as  $\bar{t} \sim 0$ ; therefore, the curvature of the temperature profile remains zero for all time, implying that the solution for the temperature can be written as  $\bar{T}(\bar{x}, \bar{t}) = -G(\bar{t})(\bar{s}(\bar{t}) - \bar{x})$ , where the temperature gradient  $G$  is to be determined. The energy balance (30a) gives that the flux is constant in space to leading order and from the Newton condition we find that  $\bar{q}(\bar{x}, \bar{t}) = -1 + G(\bar{t})\bar{s}(\bar{t})$ . Using the solutions for the temperature and the flux in the GK equation gives an evolution equation for  $G$ , which, when coupled with the Stefan condition, results in a two-dimensional system of nonlinear ODEs given by

$$\frac{dG}{d\bar{t}} = 1 - (\bar{s}(\bar{t}) + \alpha)G(\bar{t}), \quad (32a)$$

$$\frac{d\bar{s}}{d\bar{t}} = 1 - G(\bar{t})\bar{s}(\bar{t}). \quad (32b)$$

Initial conditions are given by  $G(0) = 0$  and  $\bar{s}(0) = 0$ .

To understand the dynamics that occur in the fourth time regime, it is insightful to first consider the case when  $\alpha \ll 1$ . Subtraction of the evolution equations (32) followed by integration in time shows that  $G(\bar{t}) = \bar{s}(\bar{t})$ ; hence, the Stefan condition becomes  $d\bar{s}/d\bar{t} = 1 - \bar{s}^2$ , which can be solved to find that

$$\bar{s}(\bar{t}) = \tanh \bar{t}. \quad (33)$$



Interestingly, the position of the solidification front reaches a steady state given by  $\bar{s}^* = 1$ , signifying the end of the solidification process in this time regime. To capture the additional solidification that occurs, we can introduce a fifth time regime by scaling the original dimensionless variables as  $t = \ell^2 \check{t}$ ,  $x = \ell \beta^{-1/2} \check{x}$ ,  $s = \ell \beta^{-1/2} \check{s}$ ,  $T = \check{T}$ , and  $q = \ell^{-1} \beta^{1/2} \check{q}$ . The leading-order energy and GK equations are given by  $\partial \check{q} / \partial \check{x} = 0$  and

$$\check{q} + \frac{\partial \check{T}}{\partial \check{x}} = -\frac{\partial}{\partial \check{t}} \left( \frac{\partial \check{T}}{\partial \check{x}} \right), \quad (34)$$

respectively. The rescaled Stefan condition is  $d\check{s}/d\check{t} = -\check{q}(\check{s}(\check{t}), \check{t})$ . The Newton boundary condition reduces to  $\check{T}(0, \check{t}) = -1$ . Solving this system with the matching conditions  $\check{T} \sim -1 + \check{x}$  and  $\check{s} \sim 1$  as  $\check{t} \sim 0$  shows that the temperature is in its quasi-steady profile given by  $\check{T}(\check{x}, \check{t}) = -1 + \check{x}/\check{s}(\check{t})$ . Using this temperature profile in the GK equation (34) provides the solution for the flux,  $\check{q} = -1/\check{s} + (1/\check{s}^2)(d\check{s}/d\check{t})$ , which yields a Stefan condition of the form

$$\frac{d\check{s}}{d\check{t}} = \frac{\check{s}(\check{t})}{1 + \check{s}(\check{t})^2}. \quad (35)$$

Solving this equation with the initial condition  $\check{s}(0) = 1$  results in an implicit expression for the solidification front,

$$\frac{1}{2} \check{s}(\check{t})^2 + \log \check{s}(\check{t}) = \check{t} + \frac{1}{2}, \quad (36)$$

which can be written in terms of the LambertW function as  $\check{s}(\check{t}) = [\text{W}(e^{2\check{t}+1})]^{1/2}$ .

Equations (33) and (36) can be directly obtained from (32) by considering a matched asymptotic expansion in terms of  $\alpha \ll 1$ . Seeking a solution of the form  $G(t) = G_0(\bar{t}) + O(\alpha)$  and  $\bar{s}(\bar{t}) = \bar{s}_0(\bar{t}) + O(\alpha)$  in (32) results in  $G_0(t) = \bar{s}_0(\bar{t}) = \tanh \bar{t}$ , i.e., (33). Rescaling time as  $t = \alpha^{-1} \tau$  and writing  $G(t) = \tilde{G}_0(\tau) + O(\alpha)$  and  $\bar{s}(t) = \tilde{s}_0(\tau) + O(\alpha)$  in (32) leads to the relations  $\tilde{G}_0(\tau) = 1/\tilde{s}_0(\tau)$  and  $d(\tilde{G}_0 - \tilde{s}_0)/d\tau = \tilde{G}_0$ . These can be combined into  $d\tilde{s}_0/d\tau = \tilde{s}_0/(1 + \tilde{s}_0^2)$ , which, upon solving, yields (36). In fact, this result is not surprising, since the scales that have been used for time in the fourth and fifth time regimes differ only by a factor of  $\alpha^{-1}$ . Therefore, as  $\alpha$  increases, the separation between the fourth and fifth time scales decreases. When  $\alpha = O(1)$ , these two regimes are blended together, as shown in Fig. 3 (a).

The evolution of the mean temperature gradient is shown in Fig. 3 (b) for two values of the MFP  $\ell$  with  $\gamma = 1$ ,  $\varepsilon = 10^{-3}$ , and  $\beta = 10$ . Lines correspond to the numerical solutions of the full model (7); stars, diamonds, circles, and triangles represent the asymptotic solutions in second, third, fourth, and fifth regimes, respectively. Due to the large effective thermal conductivity  $\ell^2/\gamma$ , the temperature gradient that is induced by the initial cooling of the solid in the first regime (not shown) is very small. The magnitude of the temperature gradient is consistent with the scaling estimate of  $\langle \partial T / \partial x \rangle = O(\gamma \ell^{-2})$  obtained from (28). As  $t$  becomes  $O(1)$  in size, the third time regime is entered and the temperature gradient undergoes a sustained increase until the transition between the fourth ( $t = O(\ell \beta^{1/2})$ ) and fifth ( $t = O(\ell^2)$ ) time regimes. The increase

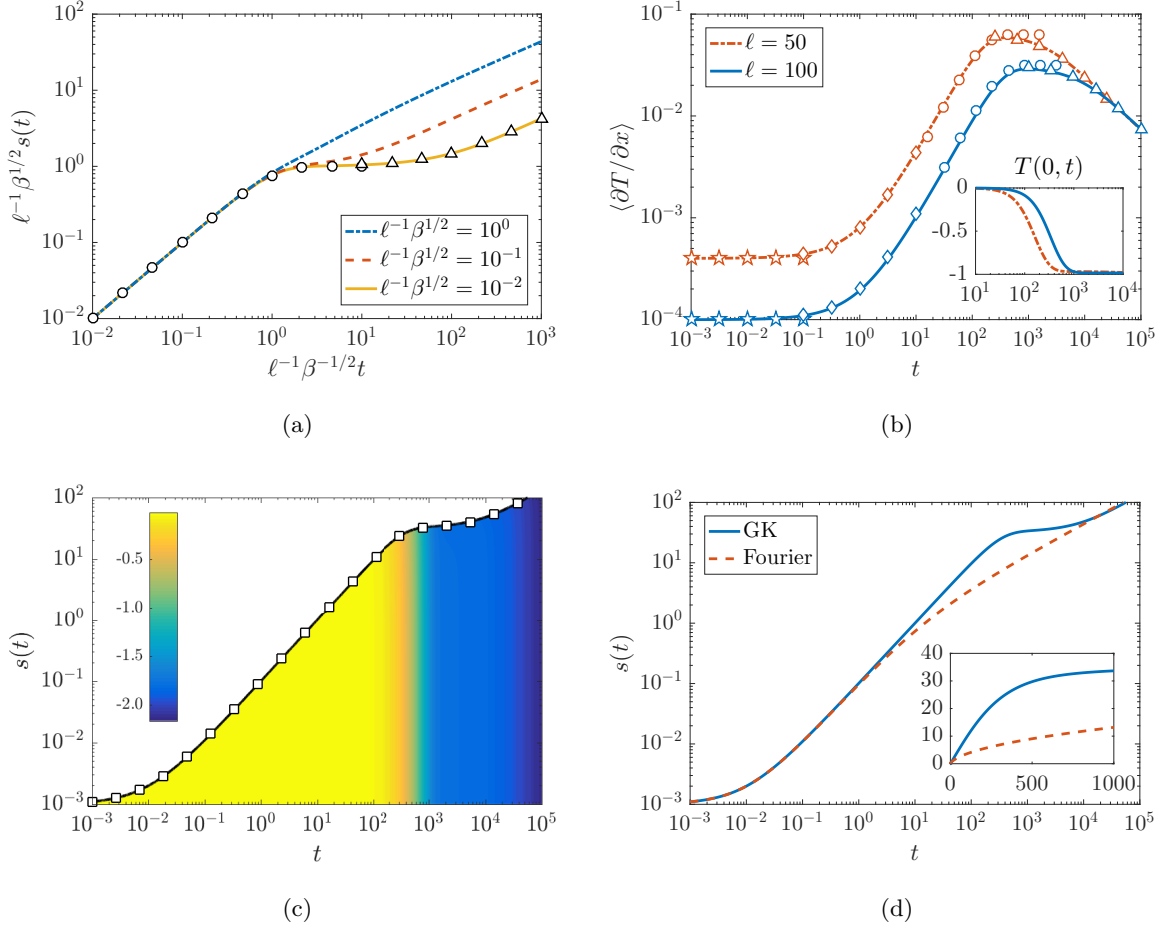


**Figure 3:** Solidification dynamics in the limit of large MFP and Stefan number. (a): The blending of the fourth and fifth time regimes as the parameter  $\ell^{-1}\beta^{1/2}$  increases. (b): Evolution of the mean temperature gradient (main panel) and the temperature at the boundary in contact with the cold environment (inset). (c): Comparison of a numerical simulation of the full model (solid lines) with the composite asymptotic solution (squares) given by (37). The superposed colour gradient represents the logarithm of the flux,  $\log_{10}(-q)$ . (d): Evolution of the solidification front as predicted from the GK (solid) and Fourier (dashed) models. The inset and main panel are the same except for the axes scalings. Lines represent numerical solutions of (32) while stars, diamonds, circles and triangles correspond to asymptotic solutions in the second, third, fourth, and fifth time regimes, respectively. Parameter values used in panels (b) and (c) are  $\gamma = 1$ ,  $\varepsilon = 10^{-3}$ ,  $\beta = 10$ , and  $\ell = 100$ .

in temperature gradient can be conceptualised in terms of the effective thermal conductivity, which decreases to the bulk value as the solid grows in size. The maximum gradient occurs when the region of solid in contact with the cold environment obtains the same temperature as the cold environment, as shown in the inset of Fig. 3 (b). The subsequent decrease in gradient is driven by the growth of the solid, since the temperatures of the solid at its boundaries remain constant in time.

Figure 3 (c) provides a comparison between the position of the solidification front that has been computed from a numerical simulation of the full model (7) and the composite asymptotic solution

$$s(t) = \varepsilon + \ell\beta^{-1/2} \tanh(\ell^{-1}\beta^{-1/2}t) + \ell\beta^{-1/2}[\mathbf{W}(e^{2t/\ell^2+1})]^{1/2} - \ell\beta^{-1/2}. \quad (37)$$

The agreement between numerics and asymptotics is excellent. The figure clearly shows a temporary decrease in the rate of front propagation, which coincides with a marked decrease in the magnitude of the thermal flux (shown as the superposed colour gradient). This decrease in flux is due a transition between energy transport mechanisms as the fifth time regime is entered.

The key difference between the fourth and fifth time regimes is the dominant mechanism of energy transport. In the fourth time regime, the flux is primarily driven by temporal changes in the temperature gradient rather than the temperature gradient itself; this is easily seen by taking  $\alpha \rightarrow 0$  in the leading-order part of the GK equation (30b). The decreasing growth of the temperature gradient (see Fig. 3 (b)) diminishes the strength of the primary mechanism of heat transport, leading to the termination of the solidification process in this regime, which coincides with the temperature gradient becoming stationary. In the fifth time regime, the flux is driven by the temperature gradient over large time scales; see (34). Thus, the temperature gradient provides a persistent mode of energy transport that can sustain the solidification process, even after the temperature profile settles into a slowly evolving quasi-steady state.

Figure 3 (d) compares the positions of the solidification front that have been computed using the GK equation (solid line) and Fourier's law (dashed line) for the thermal flux. The inset plots the same results using linear axes. Despite the slowing of front propagation that occurs in the GK model, strong non-local effects lead to a prolonged period where the growth of the solid is approximately linear, leading to a solidification process that is accelerated in comparison to the case of pure Fourier conduction. Using the simulation parameters  $\ell = 100$  and  $\beta = 10$ , the transition from linear growth kinetics occurs in the GK model when  $t \simeq 316 = O(\ell\beta^{1/2})$ ; in the case of Fourier's law, this occurs when  $t \simeq 10 = O(\beta)$ . Interestingly, the gains that are made in the solidification process during the extended period of linear growth are almost exactly offset by the slowing that occurs during the transition into the diffusion-dominated third time regime. From Fig. 3 (d), it is seen that the two curves eventually collapse onto each other, indicating the recovery of the usual quasi-steady  $s \sim (2t)^{1/2}$  solidification kinetics.

### 3.3 Limit of large relaxation time

We now study the dynamics in the asymptotic limit  $\gamma \rightarrow \infty$  and  $\beta \rightarrow \infty$ , focusing on the case when  $\beta \ll \gamma$  with  $\varepsilon \ll \gamma^{-1}$ , which leads to substantial departures from classical solidification kinetics.

The problem can be decomposed into five distinct time regimes. The first two, defined by  $t = O(\gamma\varepsilon^2)$  and  $t = O(\beta\varepsilon)$ , describe the dynamics that occur on length scales associated with the seed crystal, namely, the initial transport of heat to the environment and growth of the solid. The third time regime occurs when  $t = O(\beta\gamma^{-1})$  and, although the dynamics are dominated by non-classical effects, the thermal flux is driven by temperature gradients. This results in a change of solidification kinetics from  $s \sim t$  to  $s \sim t^{1/2}$ . In the fourth time regime,  $t = O(1)$ , the flux becomes dependent on the temperature gradient as well as the history of the temperature gradient, resulting in further changes to the solidification kinetics. Finally, in the fifth regime,  $t = O(\gamma)$ , non-local effects become negligible and the model reduces to a quasi-static version of the hyperbolic heat equation. On even longer time scales,  $t \gg \gamma$ , the system tends to the classical limit.

*First and second time regimes:* The first two time regimes are mathematically identical to those previously considered when  $\gamma = O(1)$ . The limiting behaviour of the solutions is given by  $T \sim \gamma\ell^{-2}(x - s(t))$ ,  $q \sim -1$ , and  $s \sim \beta^{-1}t$  for  $\beta\varepsilon \ll t \ll \beta\gamma^{-1}$ . The upper bound on time ensures that the temperature is small in these two regimes.

*Third time regime:* The third time regime,  $t = O(\beta\gamma^{-1})$ , accounts for  $O(1)$  temperatures and can be identified from the limiting behaviour in the second time regime. Balancing terms in the Newton condition shows that  $q = O(1)$ , which, in turn, can be used in the Stefan condition to obtain a length scale of  $O(\gamma^{-1})$ . Thus, the variables are rescaled according to  $t = \beta\gamma^{-1}\bar{t}$ ,  $x = \gamma^{-1}\bar{x}$ ,  $s = \gamma^{-1}\bar{s}$ ,  $T = \bar{T}$ , and  $q = \bar{q}$ , resulting in bulk equations given by

$$\frac{\partial \bar{q}}{\partial \bar{x}} = O(\beta^{-1}), \quad (38a)$$

$$\frac{\partial \bar{q}}{\partial \bar{t}} + \beta\gamma^{-1} \frac{\partial \bar{T}}{\partial \bar{x}} = -\ell^2 \frac{\partial}{\partial \bar{t}} \left( \frac{\partial \bar{T}}{\partial \bar{x}} \right) + O(\beta\gamma^{-2}). \quad (38b)$$

The boundary and Stefan conditions are  $\bar{q}(0, \bar{t}) = -(1 + \bar{T}(0, \bar{t}))$ ,  $\bar{T}(\bar{s}(\bar{t}), \bar{t}) = 0$ , and  $d\bar{s}/d\bar{t} = -\bar{q}(\bar{s}(\bar{t}), \bar{t})$ , with matching conditions given by  $\bar{T} \sim \ell^{-2}(\bar{x} - \bar{s}(\bar{t}))$  and  $\bar{s} \sim \bar{t}$  as  $\bar{t} \sim 0$ . The leading-order part of the GK equation (38b) can be integrated in time, yielding  $\bar{q} = -\ell^2 \partial \bar{T} / \partial \bar{x}$ , thus recovering a form of Fourier's law. Upon solving a classical problem for the temperature, one finds that

$$\bar{T}(\bar{x}, \bar{t}) = \frac{\bar{x} - \bar{s}(\bar{t})}{\bar{s}(\bar{t})^2 + \ell^2}, \quad \bar{q}(\bar{x}, \bar{t}) = -\frac{\ell^2}{\bar{s}(\bar{t})^2 + \ell^2}, \quad (39a)$$

where the position of the solidification front is determined from the positive root of

$$2\bar{s}(\bar{t}) + \ell^{-2}\bar{s}(\bar{t})^2 = 2\bar{t}. \quad (39b)$$

The small- and large-time limits of (39b) are  $\bar{s} \sim \bar{t}$  and  $\bar{s} \sim \ell(2\bar{t})^{1/2}$ , respectively, which indicate that a reduction in the rate of solidification occurs in this time regime. This slowing is attributed to the weakening of the temperature gradient and thus the thermal flux, as seen from the limits  $\bar{T} \sim -1 + \bar{x}/\bar{s}(\bar{t})$  and  $\bar{q} \sim -\ell^2/\bar{s}(\bar{t})$  for  $\bar{t} \gg 1$ .

*Fourth time regime:* The diminishing flux and temperature gradient result in additional transport mechanisms becoming relevant in the GK equation (38b). The limiting behaviour of the solution in the third time regime determines the scales for space, temperature, and flux. The time scale of  $t = O(1)$  is chosen so that the temperature gradient appears in the leading-order GK equation. The corresponding rescaling is given by  $t = \tilde{t}$ ,  $x = \beta^{-1/2}\gamma^{-1/2}\tilde{x}$ ,  $s = \beta^{-1/2}\gamma^{-1/2}\tilde{s}$ ,  $T = \tilde{T}$ , and  $q = \beta^{1/2}\gamma^{-1/2}\tilde{q}$ . The rescaled energy balance and GK equation are given by

$$\frac{\partial \tilde{q}}{\partial \tilde{x}} = O(\beta^{-1}), \quad (40a)$$

$$\frac{\partial \tilde{q}}{\partial \tilde{t}} + \gamma^{-1}\tilde{q} + \frac{\partial \tilde{T}}{\partial \tilde{x}} = -\ell^2 \frac{\partial}{\partial \tilde{t}} \left( \frac{\partial \tilde{T}}{\partial \tilde{x}} \right), \quad (40b)$$

which have boundary conditions  $\tilde{T}(0, \tilde{t}) = -1 + O(\beta^{1/2}\gamma^{-1/2})$  and  $\tilde{T}(\tilde{s}(\tilde{t}), \tilde{t}) = 0$ . The Stefan condition is  $d\tilde{s}/d\tilde{t} = -\tilde{q}(s(\tilde{t}), \tilde{t})$ . Matching conditions are  $\tilde{T} \sim -1 + \tilde{x}/\tilde{s}(\tilde{t})$ ,  $\tilde{q} \sim -\ell(2\tilde{t})^{-1/2}$ , and  $\tilde{s} \sim \ell(2\tilde{t})^{1/2}$  as  $\tilde{t} \sim 0$ . Integrating the leading-order GK equation (40b) in time results in

$$\tilde{q} = -\ell^2 \frac{\partial \tilde{T}}{\partial \tilde{x}} - \int_0^{\tilde{t}} \frac{\partial \tilde{T}}{\partial \tilde{x}} d\tilde{t}', \quad (41)$$

clearly showing the dependence of the flux on the history of the temperature gradient. To make further progress, the GK equation (40b) is differentiated with respect to  $\tilde{x}$  and the energy equation (40a) together with the boundary and matching conditions are used to show that the temperature is  $\tilde{T}(\tilde{x}, \tilde{t}) = -1 + \tilde{x}/\tilde{s}(\tilde{t})$ . Inserting the expression for the temperature in the leading-order part of the GK equation (40b) leads to a coupled system of equations for the flux and position of the solidification front:

$$\frac{d\tilde{q}}{d\tilde{t}} = -\frac{1}{\tilde{s}} - \left( \frac{\ell}{\tilde{s}} \right)^2 \tilde{q}, \quad (42a)$$

$$\frac{d\tilde{s}}{d\tilde{t}} = -\tilde{q}, \quad (42b)$$

with  $\tilde{q} \sim -\ell(2\tilde{t})^{-1/2}$  and  $s \sim \ell(2\tilde{t})^{1/2}$  for  $\tilde{t} \sim 0$ . For small times, (42a) reduces to  $d\tilde{q}/d\tilde{t} \sim -(l/\tilde{s})^2\tilde{q}$ , showing that the flux increases in time (recall that  $\tilde{q} < 0$ ). However, for large times,  $d\tilde{q}/d\tilde{t} \sim -1/\tilde{s}$ , corresponding to a decreasing flux. The non-monotonicity of the flux corresponds to a change in the dominant mechanism of thermal transport. For  $\tilde{t} \ll 1$ , the flux is driven by the temperature gradient; for  $\tilde{t} \gg 1$ , it is driven by memory effects and the history of the temperature gradient, leading to markedly different long-term solidification kinetics given by  $d\tilde{s}/d\tilde{t} \sim [2 \log(\tilde{s}/S)]^{1/2}$ , where  $S = \ell^2(\pi/2)^{1/2}$ .

*Fifth time regime:* The sustained growth of the solid beyond the dimensions of the phonon MFP reduces the influence of non-local effects. The fifth time regime describes the evolution of

the solidification process in the absence of such effects. The associated scales for the variables can be determined from the GK equation in the fourth time regime (40b), which shows that a different balance occurs when  $\tilde{x}, \tilde{t} = O(\gamma)$ . The original dimensionless variables are therefore scaled as  $t = \gamma \hat{t}$ ,  $x = \beta^{-1/2} \gamma^{1/2} \hat{x}$ ,  $s = \beta^{-1/2} \gamma^{1/2} \hat{s}$ ,  $T = \hat{T}$ , and  $q = \beta^{1/2} \gamma^{-1/2} \hat{q}$ , leading to bulk equations given by

$$\frac{\partial \hat{q}}{\partial \hat{x}} = O(\beta^{-1}), \quad (43a)$$

$$\frac{\partial \hat{q}}{\partial \hat{t}} + \hat{q} + \frac{\partial \hat{T}}{\partial \hat{x}} = O(\gamma^{-1}), \quad (43b)$$

corresponding to the quasi-static hyperbolic heat equation. The leading-order boundary conditions are  $\hat{T}(0, \hat{t}) = -1$  and  $\hat{T}(\hat{s}(\hat{t}), \hat{t}) = 0$ . Differentiation of (43b) with respect to  $\hat{x}$  and using (43a) along with the boundary conditions shows that  $\hat{T} = -1 + \hat{x}/\hat{s}(\hat{t})$ . The problem then reduces to a system of differential equations for the flux and position of the solidification front given by

$$\frac{d\hat{q}}{d\hat{t}} + \hat{q} = -\frac{1}{\hat{s}}, \quad (44a)$$

$$\frac{d\hat{s}}{d\hat{t}} = -\hat{q}. \quad (44b)$$

For  $\hat{t} \ll 1$ , we find that  $d\hat{q}/d\hat{t} \sim -1/\hat{s}$ , consistent with the limiting behaviour in the fourth regime. For large times,  $\hat{t} \gg 1$ , we have  $\hat{q} \sim -1/\hat{s}$  and thus  $\hat{s} \sim (2\hat{t})^{1/2}$ , recovering the classical solidification kinetics as the flux once again becomes primarily driven by temperature gradients.

Figure 4 shows the evolution of the temperature gradient (panel(a)), flux (panel (b)), and the position of the solidification front (panel (c)) in the case of  $\beta = 10$ ,  $\gamma = 250$ ,  $\ell = 1$ , and  $\varepsilon = 10^{-5}$ . Although these parameters lie outside of the estimates given in Sec. 2.7, they provide sufficient time-scale separation to illustrate the range of behaviour that occurs across the various regimes. In Fig. 4, the solid line corresponds to the numerical solution of the full model (7). Diamonds and circles denote the asymptotic solutions in the second and third regime, and squares, triangles and stars represent numerical solutions of the reduced model in the first, fourth, and fifth regime, given by (13), (42) and (44), respectively. Obtaining a precise matching condition for (44) was not possible and thus it was patched to the numerical solution in the fourth regime. The asymptotic solutions capture the qualitative trend seen in the numerical simulation and the error is consistent with the magnitude of the  $O(\beta^{1/2} \gamma^{-1/2})$  terms that are neglected when analysing the model in the fourth time regime. Despite these errors, the asymptotic solution for the position of the solidification front is in good agreement with the numerical simulation.

The dashed lines in Fig. 4 correspond to the temperature gradient, flux, and position of the solidification front computed from Fourier's law and highlight the vastly different dynamics that occur when the relaxation time is large. The small effective thermal conductivity  $\ell^2/\gamma$  leads to the rapid development of large temperature gradients in the first time regime,  $t \simeq$

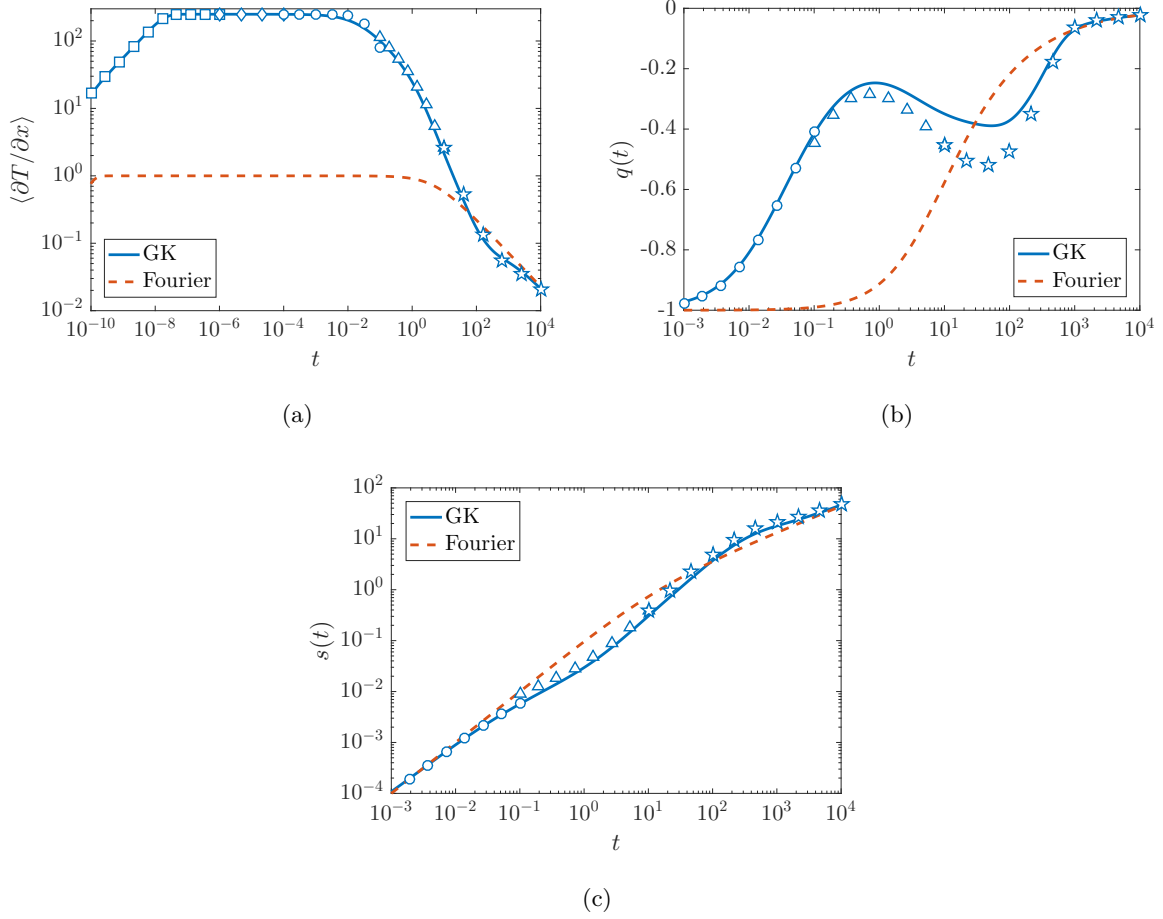


**Figure 4:** Solidification dynamics in the limit of large relaxation time and Stefan number. Comparisons of the temperature gradient (a), flux (b), and position of the solidification front (c) from the GK (solid line) and Fourier (dashed line) models. Diamonds and circles denote asymptotic solutions in the second and third regimes; squares, triangles, and stars represent numerical solutions of the reduced models in the first, fourth, and fifth regimes given by (13), (42), and (44), respectively. Note that  $q(t)$  is calculated from the full model by taking the integrated average of  $q(x, t)$  in space. Parameter values are  $\beta = 10$ ,  $\gamma = 250$ ,  $\ell = 1$ , and  $\varepsilon = 10^{-5}$ .

$10^{-8} = O(\gamma\varepsilon^2)$ , which are constant throughout the second time regime,  $t \simeq 10^{-4} = O(\beta\varepsilon)$ . The third time regime,  $t \simeq 10^{-2} = O(\beta\gamma^{-1})$ , captures the decrease in thermal flux that occurs as a result of the poor effective thermal conductivity. As Fig. 4 (c) shows, the diminished transport of thermal energy in the third time regime leads to an earlier transition to slower  $s \sim t^{1/2}$  solidification kinetics compared to the Fourier case. However, as the system enters the fourth time regime,  $t = O(1)$ , the history of the temperature gradient becomes similar in magnitude to the instantaneous value of the temperature gradient, and this extra contribution to the thermal flux leads to enhanced energy transport and a sustained acceleration of the solidification process. In the fifth time regime,  $t \simeq 10^2 = O(\gamma)$ , these memory effects become sub-dominant and the flux, once again, becomes driven by temperature gradients with a thermal conductivity that coincides with the bulk value, recovering the classical solidification kinetics.

## 4 Discussion and conclusion

The asymptotic analysis reveals that a form of Fourier’s law, with an effective thermal conductivity depending on the non-classical parameters, is recovered on small time scales. On large time scales, the weakening of non-classical transport mechanisms leads to a recovery of the classical form of Fourier’s law, based on the bulk thermal conductivity of the material. These results highlight the size-dependent nature of the thermal conductivity of nanomaterials and support the idea that, in certain regimes, nanoscale heat conduction can be described by Fourier’s law if a suitable choice of thermal conductivity is made [37, 38, 62–64].

Key differences in the dominant transport mechanism across intermediate time scales are observed when the relaxation time and phonon MFP are large. In the former case, the flux is driven by the history (integral in time) of the temperature gradient. This is in perfect contrast to the latter case, where the flux is driven by the instantaneous rate of change (time derivative) of the temperature gradient. Despite these seemingly opposite relationships between the flux and temperature gradient, both lead to an enhancement of energy transport across the solid and a non-trivial increase in the rate of solidification.

The focus on solidification in the limit of large Stefan number is to facilitate the asymptotic analysis. However, a numerical study of the model with  $O(1)$  Stefan numbers indicates the same qualitative behaviours occur. This similarity is explained by the fact that  $O(1)$  Stefan numbers do not change the ordering of the time regimes identified by the asymptotic analysis. Physically, it means that the rate of solidification does not alter the sequence of dominant thermal transport mechanisms; rather, it only affects when the transition between these mechanisms takes place.

In classical models of phase change, the governing equations for melting and solidification are the same. Thus, theoretical insights into one process can be applied to the other. The GK equation, which can be derived from the framework of extended irreversible thermodynamics [33], in principle, can be used to describe the flux of thermal energy in the liquid phase. However,



much less is known about the precise mechanism of thermal transport in nanoscale liquids and phonon-based theories are still being developed [65]. A difference between thermal transport mechanisms in solids and liquids would break the analogy between solidification and melting, thereby preventing the results from this study to be applied to the problem of nanoscale melting.

By studying a simple model with asymptotic techniques, we are able to obtain novel insights into how solidification is affected by non-Fourier heat conduction. Although motivated by applications in nanotechnology, the model and analysis can be used more generally to describe rapid solidification processes occurring on time and length scales that are commensurate with the thermal relaxation time and phonon mean free path of a material.

## Acknowledgements

We thank Brian Wetton for his advice regarding the numerical solution of this problem. This project has received funding from the European Union's Horizon 2020 research and innovation programme under grant agreement No 707658. MC acknowledges that the research leading to these results has received funding from 'la Caixa' Foundation. TGM acknowledges the support of a Ministerio de Ciencia e Innovación grant MTM2014-56218. The authors have been partially funded by the CERCA Programme of the Generalitat de Catalunya.

## References

- [1] E. C. Garnett, M. L. Brongersma, Y. Cui, and M. D. McGehee. Nanowire solar cells. *Annu. Rev. Mater. Res.*, 41:269–295, 2011.
- [2] J. Wang. Carbon-nanotube based electrochemical biosensors: A review. *Electroanal.*, 17(1):7–14, 2005.
- [3] O. V. Salata. Applications of nanoparticles in biology and medicine. *J. Nanobiotechnol*, 2(1):3, 2004.
- [4] C. Mah, I. Zolotukhin, T. J. Fraites, J. Dobson, C. Batich, and B. J. Byrne. Microsphere-mediated delivery of recombinant AAV vectors in vitro and in vivo. *Mol. Ther.*, 1(5):S239–S242, 2000.
- [5] J.-M. Nam, C. S. Thaxton, and C. A. Mirkin. Nanoparticle-based bio-bar codes for the ultrasensitive detection of proteins. *Science*, 301(5641):1884–1886, 2003.
- [6] J. Ma, H. Wong, L. B. Kong, and K.-W. Peng. Biomimetic processing of nanocrystallite bioactive apatite coating on titanium. *Nanotechnology*, 14(6):619, 2003.
- [7] E. Pop, S. Sinha, and K. E. Goodson. Heat generation and transport in nanometer-scale transistors. *P. IEEE*, 94(8):1587–1601, 2006.

- [8] B. Poudel, Q. Hao, Y. Ma, Y. Lan, A. Minnich, B. Yu, X. Yan, D. Wang, A. Muto, D. Vashaee, X. Chen, J. Liu, M. S. Dresselhaus, G. Chen, and Z. Ren. High-thermoelectric performance of nanostructured bismuth antimony telluride bulk alloys. *Science*, 320(5876): 634–638, 2008. ISSN 0036-8075. doi: 10.1126/science.1156446. URL <http://science.sciencemag.org/content/320/5876/634>.
- [9] K. Hamad-Schifferli, J. J. Schwartz, A. T. Santos, S. Zhang, and J. M. Jacobson. Remote electronic control of dna hybridization through inductive coupling to an attached metal nanocrystal antenna. *Nature*, 415(6868):152–155, 2002.
- [10] D. G. Cahill, W. K. Ford, K. E. Goodson, G. D. Mahan, A. Majumdar, H. J. Maris, R. Merlin, and S. R. Phillpot. Nanoscale thermal transport. *J. Appl. Phys.*, 93(2):793–818, 2003.
- [11] M. E. Siemens, Q. Li, R. Yang, K. A. Nelson, E. H. Anderson, M. M. Murnane, and H. C. Kapteyn. Quasi-ballistic thermal transport from nanoscale interfaces observed using ultrafast coherent soft x-ray beams. *Nat. Mater.*, 9(1):26–30, 2010.
- [12] D. G. Cahill, P. V. Braun, G. Chen, D. R. Clarke, S. Fan, K. E. Goodson, P. Keblinski, W. P. King, G. D. Mahan, A. Majumdar, H. J. Maris, S. R. Phillpot, E. Pop, and L. Shi. Nanoscale thermal transport. ii. 2003–2012. *Appl. Phys. Rev.*, 1(1):011305, 2014.
- [13] A. Nie, J. Liu, C. Dong, and H. Wang. Electrical failure behaviors of semiconductor oxide nanowires. *Nanotechnology*, 22(40):405703, 2011.
- [14] P. Buffat and J. P. Borel. Size effect on the melting temperature of gold particles. *Phys. Rev. A*, 13(6):2287, 1976.
- [15] T. B. David, Y. Lereah, G. Deutscher, R. Kofman, and P. Cheyssac. Solid-liquid transition in ultra-fine lead particles. *Philos. Mag. A*, 71(5):1135–1143, 1995.
- [16] C. R. M. Wronski. The size dependence of the melting point of small particles of tin. *Brit. J. Appl. Phys.*, 18(12):1731, 1967.
- [17] S. L. Lai, J. Y. Guo, V. Petrova, G. Ramanath, and L. H. Allen. Size-dependent melting properties of small tin particles: nanocalorimetric measurements. *Phys. Rev. Lett*, 77(1): 99, 1996.
- [18] M. Zhang, M. Y. Efremov, F. Schiettekatte, E. A. Olson, A. T. Kwan, S. L. Lai, T. Wisleder, J. E. Greene, and L. H. Allen. Size-dependent melting point depression of nanostructures: nanocalorimetric measurements. *Phys. Rev. B*, 62(15):10548, 2000.
- [19] J. Sun and S. L. Simon. The melting behavior of aluminum nanoparticles. *Thermochim. Acta*, 463(1):32–40, 2007.

- [20] R. C. Tolman. The effect of droplet size on surface tension. *J. Chem. Phys.*, 17(3):333–337, 1949.
- [21] C.-W. Chang, D. Okawa, H. Garcia, A. Majumdar, and A. Zettl. Breakdown of Fourier’s law in nanotube thermal conductors. *Phys. Rev. Lett.*, 101(7):075903, 2008.
- [22] D. Li, Y. Wu, P. Kim, L. Shi, P. Yang, and A. Majumdar. Thermal conductivity of individual silicon nanowires. *Appl. Phys. Lett.*, 83(14):2934–2936, 2003.
- [23] J. A. Johnson, A. A. Maznev, J. Cuffe, J. K. Eliason, A. J. Minnich, T. Kehoe, C. M. S. Torres, G. Chen, and K. A. Nelson. Direct measurement of room-temperature nondiffusive thermal transport over micron distances in a silicon membrane. *Phys. Rev. Lett.*, 110(2):025901, 2013.
- [24] J. M. Back, S. W. McCue, and T. J. Moroney. Including nonequilibrium interface kinetics in a continuum model for melting nanoscaled particles. *Sci. Rep.*, 4, 2014.
- [25] F. Font and T. G. Myers. Spherically symmetric nanoparticle melting with a variable phase change temperature. *J. Nanopart. Res.*, 15(12):2086, 2013.
- [26] F. Font, T. G. Myers, and S. L. Mitchell. A mathematical model for nanoparticle melting with density change. *Microfluid. Nanofluid.*, 18(2):233–243, 2015.
- [27] S. W. McCue, B. Wu, and J. M. Hill. Micro/nanoparticle melting with spherical symmetry and surface tension. *IMA J. Appl. Math.*, 74(3):439–457, 2008.
- [28] T. G. Myers and F. Font. On the one-phase reduction of the Stefan problem with a variable phase change temperature. *Int. Commun. Heat Mass*, 61:37–41, 2015.
- [29] H. Ribera and T. G. Myers. A mathematical model for nanoparticle melting with size-dependent latent heat and melt temperature. *Microfluid. Nanofluid.*, 20(11):147, 2016.
- [30] B. J. Florio and T. G. Myers. The melting and solidification of nanowires. *J. Nanopart. Res.*, 18(6):1–12, 2016.
- [31] G. K. Goswami and K. K. Nanda. Size-dependent melting of finite-length nanowires. *The Journal of Physical Chemistry C*, 114(34):14327–14331, 2010.
- [32] T. G. Myers. Mathematical modelling of phase change at the nanoscale. *Int. Commun. Heat Mass*, 76:59–62, 2016.
- [33] D. Jou, J. Casas-Vázquez, and G. Lebon. *Extended Irreversible Thermodynamics*. Springer, fourth edition, 2010.
- [34] C. Cattaneo. A form of heat conduction equation which eliminates the paradox of instantaneous propagation. *Compte Rendus*, 247(4):431–433, 1958.

- [35] R. A. Guyer and J. A. Krumhansl. Solution of the linearized phonon boltzmann equation. *Phys. Rev.*, 148(2):766, 1966.
- [36] R. A. Guyer and J. A. Krumhansl. Thermal conductivity, second sound, and phonon hydrodynamic phenomena in nonmetallic crystals. *Phys. Rev.*, 148(2):778, 1966.
- [37] F. X. Alvarez, D. Jou, and A. Sellitto. Phonon hydrodynamics and phonon-boundary scattering in nanosystems. *J. Appl. Phys.*, 105(1):014317, 2009.
- [38] M. Calvo-Schwarzwalder, M. G. Hennessy, P. Torres, T. G. Myers, and F. X. Alvarez. A slip-based model for the size-dependent effective thermal conductivity of nanowires. *Int. Comm. Heat Mass*, 91:57–63, 2018.
- [39] P. Colli and M. Grasselli. Hyperbolic phase change problems in heat conduction with memory. *Proc. Roy. Soc. Edinb. A*, 123(3):571–592, 1993.
- [40] A. Friedman and B. Hu. The Stefan problem for a hyperbolic heat equation. *J. Math. Anal. Appl.*, 138(1):249–279, 1989.
- [41] R. E. Showalter and N. J. Walkington. A hyperbolic Stefan problem. *Q. Appl. Math.*, 45(4):769–781, 1987.
- [42] D. E. Glass, M. Necati Ozisik, S. S. McRae, and W. S. Kim. Formulation and solution of hyperbolic Stefan problem. *J. Appl. Phys.*, 70(3):1190–1197, 1991.
- [43] J. M. Greenberg. A hyperbolic heat transfer problem with phase changes. *IMA J. Appl. Math.*, 38(1):1–21, 1987.
- [44] A. D. Solomon, V. Alexiades, D. G. Wilson, and J. Drake. On the formulation of hyperbolic Stefan problems. *Q. Appl. Math.*, 43(3):295–304, 1985.
- [45] H. Liu, M. Bussmann, and J. Mostaghimi. A comparison of hyperbolic and parabolic models of phase change of a pure metal. *Int. J. Heat Mass Tran.*, 52(5):1177–1184, 2009.
- [46] M. H. Sadd and J. E. Didlake. Non-Fourier melting of a semi-infinite solid. *J. Heat Transf.*, 99(1):25–28, 1977.
- [47] A. M. Mullis. Rapid solidification within the framework of a hyperbolic conduction model. *Int. J. Heat Mass Tran.*, 40(17):4085–4094, 1997.
- [48] G.-X. Wang and V. Prasad. Microscale heat and mass transfer and non-equilibrium phase change in rapid solidification. *Mat. Sci. Eng. A-Struc.*, 292(2):142–148, 2000.
- [49] Z.-S. Deng and J. Liu. Non-Fourier heat conduction effect on prediction of temperature transients and thermal stress in skin cryopreservation. *J. Therm. Stresses*, 26(8):779–798, 2003.

- [50] H. Ahmadikia and A. Moradi. Non-Fourier phase change heat transfer in biological tissues during solidification. *Heat Mass Transfer*, 48(9):1559–1568, 2012.
- [51] A. Kumar, S. Kumar, V. K. Katiyar, and S. Telles. Phase change heat transfer during cryosurgery of lung cancer using hyperbolic heat conduction model. *Comput. Biol. Med.*, 84:20–29, 2017.
- [52] S. L. Sobolev. Two-temperature stefan problem. *Phys. Lett. A*, 197(3):243–246, 1995.
- [53] S. L. Sobolev. Local non-equilibrium transport models. *Phys. Usp.*, 40(10):1043–1053, 1997.
- [54] S. L. Sobolev. Transport processes and traveling waves in systems with local nonequilibrium. *Phys. Usp.*, 34(3):217, 1991.
- [55] S. L. Sobolev. The local-nonequilibrium temperature field around the melting and crystallization front induced by picosecond pulsed laser irradiation. *Int. J. Thermophys.*, 17(5):1089–1097, 1996.
- [56] R. Kovács and P. Ván. Generalized heat conduction in heat pulse experiments. *Int. J. Heat Mass Tran.*, 83:613–620, 2015.
- [57] A. Moosaie. Non-Fourier heat conduction in a finite medium with insulated boundaries and arbitrary initial conditions. *Int. Commun. Heat Mass*, 35(1):103–111, 2008.
- [58] P. Ván, A. Berezovski, T. Fülöp, Gy. Gróf, R. Kovács, Á. Lovas, and J. Verhás. Guyer-Krumhansl-type heat conduction at room temperature. *arXiv preprint arXiv:1704.00341*, 2017.
- [59] P. K. Galenko and D. A. Danilov. Model for free dendritic alloy growth under interfacial and bulk phase nonequilibrium conditions. *J. Cryst. Growth*, 197(4):992–1002, 1999.
- [60] C. M. Bender and S. A. Orszag. *Advanced Mathematical Methods for Scientists and Engineers I: Asymptotic Methods and Perturbation Theory*, chapter 9. Springer, 2013.
- [61] E. J. Hinch. *Perturbation Methods*, chapter 5. Cambridge University Press, 1991.
- [62] Y. Dong, B.-Y. Cao, and Z.-Y. Guo. Size dependent thermal conductivity of Si nanosystems based on phonon gas dynamics. *Physica E*, 56:256–262, 2014.
- [63] Y. Ma. Size-dependent thermal conductivity in nanosystems based on non-Fourier heat transfer. *Appl. Phys. Lett.*, 101(21):211905, 2012.
- [64] S. L. Sobolev. Nonlocal diffusion models: Application to rapid solidification of binary mixtures. *Int. J. Heat Mass Tran.*, 71:295–302, 2014.

- [65] D. Bolmatov, V. V. Brazhkin, and K. Trachenko. The phonon theory of liquid thermodynamics. *Sci. Rep.*, 2:421, 2012.